Spontaneous interlayer compression in commensurately stacked van der Waals heterostructures

Nicholas A. Pike [1,*,†] Antoine Dewandre,[1,*] François Chaltin [2] Laura Garcia Gonzalez,[3] Salvatore Pillitteri,[3]
Thomas Ratz [4] and Matthieu J. Verstraete[1,5]

[1]*nanomat/Q-MAT/CESAM and European Theoretical Spectroscopy Facility, Université de Liège, B-4000 Liège, Belgium*
[2]*Department of Chemical Engineering, Université de Liège (B6a), B-4000 Liège, Belgium*
[3]*Department of Physics, Université de Liège (B5), B-4000 Liège, Belgium*
[4]*Solid State Physics, Interfaces and Nanostructures/Q-MAT/CESAM, Université de Liège, B-4000 Liège, Belgium*
[5]*Catalan Institute of Nanoscience and Nanotechnology (ICN2), Campus UAB, Bellaterra, 08193 Barcelona, Spain*

Interest in layered two-dimensional materials, particularly stacked heterostructures of transition-metal dichalcogenides, has led to the need for a better understanding of the structural and electronic changes induced by stacking. Here, we investigate the effects of idealized heterostructuring, with periodic commensurate stacking, on the structural, electronic, and vibrational properties, when compared to the counterpart bulk transition-metal dichalcogenide. We find that in heterostructures with dissimilar chalcogen species there is a strong compression of the interlayer spacing, compared to the bulk compounds. This compression of the heterostructure is caused by an increase in the strength of the induced polarization interaction between the layers, but not a full charge transfer. We argue that this effect is real, not due to the imposed commensurability, and should be observable in heterostructures combining different chalcogens. Interestingly, we find that incommensurate stacking of Ti-based dichalcogenides can lead to the stabilization of the charge-density wave phonon mode, which is unstable in the 1T phase at low temperature. Mixed Ti- and Zr-based heterostructures are still dynamically unstable, but TiS_2/ZrS_2 becomes ferroelectric.

I. INTRODUCTION

The idea that an ordered stacking of two-dimensional (2D) materials leads to exotic electronic properties has been around since the discovery of graphene [1]. 2D materials are often used as building-blocks for "materials-by-design" [2]: Each layer displays characteristics that depend on a number of controllable factors including the chemical composition [3,4], the number of layers, and the rotation angle between individual layers [5,6]. With the increasing interest in heterostructure devices, it is important to understand, from a first-principles approach, how their structural, electronic, and vibrational properties change due to stacking. This is especially true as experimental limitations are overcome in producing large-area, transferable, monolayers (ML) of material [7] and heterostructure devices [8].

Experiments combine ML materials (graphene, black phosphorus, hexagonal boron-nitride, MoS_2, etc.) into heterostructure devices, either by creating lateral junctions via in-plane covalent bonding [9] or by growing or stacking them vertically [10]. These devices are used as biosensors [11], field-effect transistors [12], photo detectors [13], and electro-optical devices [14–17]. Cao *et al.* [18] even showed that at very small angles twisted bilayer graphene can become superconducting. Stacked heterostructures with different transition-metal dichalcogenides (TMDs) (e.g., $MoSe_2$ on WSe_2) have long-lived interlayer excitons, resulting in spatially separated electrons and holes [15,19,20], an ideal feature for photovoltaic applications. Stacking of non-TMD layered materials into incommensurate heterostructures has also been shown to lead to enhancements in the electronic specific heat of the heterostructure and stabilization of native charge density waves [21]. Low-frequency Raman measurements of heterostructure materials [22–24] can be used to determine the strength of layer interactions in a heterostructure lattice. The presence and frequency shifts of in-plane shear modes show commensurate stacking and strain effects. Even for incommensurate materials, the interlayer breathing mode is always present and its frequency and width reveal details of the layer distance and bonding strength.

Recent high-throughput calculations, see for example Refs. [25–28], have discovered numerous 2D materials that could be used to create devices with unique electric and optical properties. The combinatorial phase space for 2D heterostructures is immense and there are many unique and exotic phenomena yet to be explored both experimentally and theoretically. *Ab initio* simulations determining the properties of stacked heterostructures have expanded significantly in the past few years, but are often limited to commensurate cases, despite the large sizes of the super-lattices that are observed experimentally.

Recent work by Van Troeye *et al.* [29] on van der Waals (vdW) heterostructures used first-principles ingredients to predict the coherence of a heterostructure from the individual

———
[*]These authors contributed equally to this work.
[†]Nicholas.pike@ulg.ac.be

ML elastic constants and structural parameters. Work by Pizzi *et al.* [30] on layer-dependent interactions in stacked materials composed of the same ML used symmetry arguments and a spring model to understand layer dependent vibrational properties in vdW structures. Sohier *et al.* [31] examined the effect of dielectric heterostructuring on charge transport through explicit mutually induced electrostatics. In the hexagonal TMDs, Phillips *et al.* [32] and Terrones *et al.* [33] calculated the electronic structure of experimentally realized bilayer heterostructures in both AA and AA' stacking (known as "AB stacking" in their work) assuming a commensurate structure and found both direct and indirect electronic band gaps.

In the following, we investigate heterostructures of vertically stacked TMD materials using first-principles calculations. This approach ensures a consistent interpretation of the results across a wide variety of physical properties. In Sec. II, we describe the structure of our TMD stacks, for the two crystal symmetries used here. Section III describes our first-principles methods, and Sec. IV details and discusses the results of our calculations for all the commensurate heterostructures, in particular the interlayer compression. Finally, in Sec. V we provide concluding remarks.

II. CRYSTAL STRUCTURE

In their bulk forms, the TMD compounds are stacked layers bound by vdW forces. They belong to two main symmetry classes: hexagonal (H) ($P6_3/mmc$, space group 194) and trigonal (T) ($P\bar{3}m1$, space group 164). A few metals, such as Re, produce a closely related triclinic structure ($P\bar{1}$, space group 2). The structures are similar, with layers of trigonal or octrahedral prisms, but give different stacking orders in the bulk. An example of these two materials is shown in Fig. 1 in which the bulk structures of generic H and T TMDs are shown on the top left and the commensurately stacked heterostructures are on the bottom left. The H-TMDs have AA' stacking, as a result of the 180° rotation between the layers, and the T-TMDs have AA stacking. We denote the structures here as, e.g., $MoSe_2/WSe_2$, in the notation of Ref. [34], omitting the rotation angle between the layers. In our case, because of the imposed commensurability, this angle is always 0, but in reality many intermediate angles can be chosen, resulting in long-range moiré patterns [35,36]. Importantly, both experiments and theory [33,37] have shown that bilayer TMDs forming a moiré pattern have up to 0.5 Å of variation in the interlayer distance when the chalcogen atoms are stacked vertically (corresponding to the difference between AA' and AA stacking). The rotation angle between the layers could certainly influence the interlayer compression and modulate the electrostatic effects we find below. We preserve the natural stacking order for both H- and T-TMDs (AA' and AA respectively).

In Fig. 1 we indicate the thickness (t) and vdW gap (d) for all structural types. We define t to represent the vertical
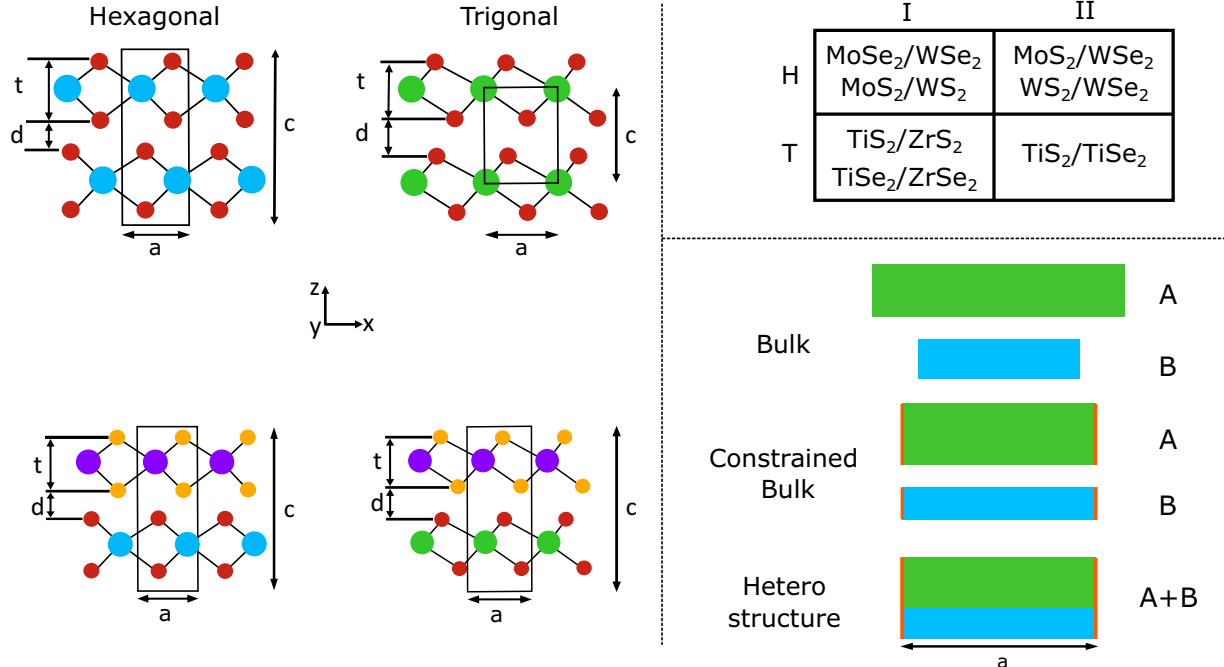
FIG. 1. Left: Sketches of bulk H-TMDs and T-TMDs with the transition-metal atoms as blue/green spheres, chalcogen atoms in red/orange spheres, and unit-cell coordinate system. The black rectangles represent the unit cells for each structure. The difference in stacking sequences for the TMDs can be observed in the lower left of the figure. H-TMDs have AA' stacking in the z direction while the T-TMDs have AA stacking in the z direction. The geometric thickness (t) and vdW gap (d) is shown in relation to the out-of-plane lattice constant (c) for all cases. Upper right: Category for each heterostructure into group I and II for each crystal symmetry. Lower right : Cartoon representation of our calculation process. Given two bulk structures, A and B in the upper right, we generate the heterostructure (A+B, lower right) and use the relaxed lattice parameters of A+B to generate the constrained bulk structures (middle right). Orange vertical bars indicate that the in-plane lattice parameters of the heterostructure and constrained calculations are identical.
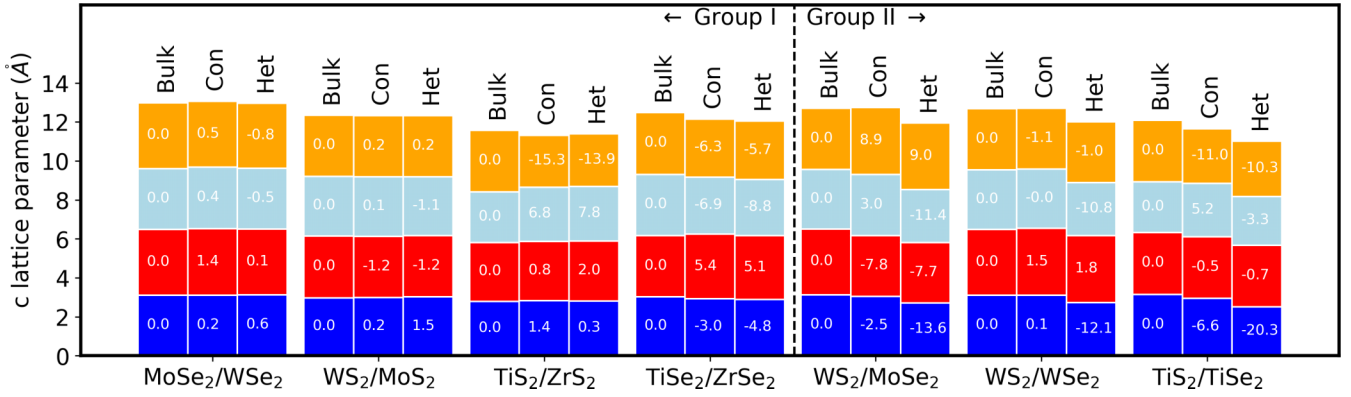
FIG. 2. The calculated out-of-plane lattice parameter (full height of each bar) for each of the heterostructures considered here are broken down into contributions from the thickness (t) of each layer (A, orange and B, red) and the vdW gap (d) for each layer (A, light blue and B, dark blue) as described in Fig. 1. For each set of three bars—Left: sum of the bulk values of t and d (Ref. [3]). Right: fully relaxed heterostructures. Middle bar: sum of constrained calculations, for each material with in-plane lattice matching the relaxed heterostructure. The inset-white numbers correspond to the percentage of compression or expansion of the individual thickness/spacing, when compared to bulk values. A and B correspond to the first and second material given in the title of each triplet of bars. There is a systematic trend to global compression, which is much stronger (up to 10% and more) in the mixed chalcogen cases (group II, right 3 sets).

distance between the outermost chalcogen atoms of an individual layer and d as the vertical distance between nearest-neighbor chalcogen atoms of different layers.

Our heterostructures are composed of two different TMD layers repeating periodically in the out-of-plane direction. The number of possible combinations is restricted by studying only combinations of compounds with the same symmetry, and including the most common TMD chemistry's. It is important to note that the T-TMD MLs possess inversion symmetry, whereas H-TMD MLs do not (only the bulk crystal does), and this carries over to the heterostructures they compose. Thus, for H-MLs stacked as a heterostructure, the space group of the heterostructure reduces to $P\bar{6}m2$ (space group 187).

III. CALCULATION METHODS

We employ density-functional theory (DFT) [38] and density-functional perturbation theory (DFPT) [39–41] calculations, as implemented in the ABINIT software package [42–45], with a plane-wave basis set and norm-conserving pseudopotentials. The pseudopotentials used here are generated using the fhi98pp code [46,47], except for W and Ti, which produced inaccurate lattice parameters (errors over 5%) or overly large band-gap energies. For W, we use a pseudopotential generated with the OPIUM code [48] and for Ti the pseudopotential is generated using the ONCVPSP software [49,50]. In all cases, the pseudopotentials use the GGA-PBE exchange-correlation functional [51] without spin-orbit coupling. In our previous work [3] we showed that the inclusion of spin-orbit interactions introduced a small splitting of the electronic bands at momentum point K with no significant contribution to the structural and vibrational properties in bulk TMD compounds, although it is very important in transport and optical properties.

Our calculations of the heterostructures follow careful convergence studies of the energy cut-off (E_{cut}) and of the reciprocal space k-point mesh for each of the compounds.

A plane-wave cutoff energy of $E_{cut} = 50$ Ha and a k-point grid size of $8 \times 8 \times 8$ ($16 \times 16 \times 8$ for the metallic TMD systems) guarantee total energies to within 3 meV per six-atom unit cell for all the compounds. The self-consistent cycle is converged to total energy differences less than 10^{-10} Ha. For the relaxation of the structural parameters we use the Broyden-Fletcher-Goldfarb-Shanno minimization procedure [52] in which we allow both the position of the atoms and cell shape to change simultaneously, while imposing symmetry. Convergence of this relaxation procedure stopped when the forces are lower than 1 μHa/Bohr. Our DFPT calculations for the interatomic force constants used the same optimized E_{cut} and the relaxed geometries. Static atomic charges are determined from a Bader atom-in-molecule approach [53] within ABINIT .

To take into account the long-range electron-electron correlation, we use the dispersion scheme given by Grimme [54], which is known to reproduce the interactions of 2D materials quite well [3,55,56]. This dispersion scheme, known as DFT-D, is based on simple atomic pair-wise terms, with environment-dependent dispersion coefficients tabulated beforehand using time-dependent DFT. We showed previously that DFT-D3 in particular is very accurate compared to experiment in the 2D TMDs [3]. More generally, the performance of the most-popular vdW functional and dispersion schemes have been assessed recently [57] and DFT-D3 performs well compared to more elaborate methods. We provide a comparison in Sec. IV C.

For all the vibrational property calculations we numerically converge the ground-state wave function to a relative variance less than 10^{-18}, and the first-order wave functions to less than 10^{-10}. The dynamical matrices are calculated on an irreducible Brillouin Zone wedge of q points corresponding to an unshifted $4 \times 4 \times 4$ mesh.

The overall calculation procedure for each heterostructure is as follows: First, we generate and fully relax the periodically stacked commensurate heterostructures A/B (third column of data in Fig. 2). These heterostructure geometries

differ from the bulk due to two main effects: the juxtaposition of the layers (both short-range "chemical" and long-range dielectric interaction), and the strain imposed by the artificial commensuration. Second, to separate these effects, we generate constrained bulk structures for each component, e.g., A, constraining the in-plane lattice parameters of a bulk unit cell of A to those of the heterostructure, and allowing the out-of-plane lattice parameter as well as the atomic positions to relax (middle bars in Fig. 2). After relaxation we calculate the electronic and vibrational properties of each heterostructure. In several cases we have calculated the properties of relaxed commensurate unsupported bilayers to compare with the full heterostructures.

IV. RESULTS

Comparing the heterostructure to isolated MLs, the relaxation of a multilayered system must account for the lattice mismatch between the individual crystalline layers. This mismatch adds a strain energy to the interface, which generically will compress one layer and expand the other. In reality, 2D vdW systems often release this strain energy by rotating one layer with respect to the other, forming commensurate long-range relaxation patterns (moiré) or incommensurate interfaces [29]. Given that our structures are forced to be commensurate, the strain energy leads to an intermediate in-plane lattice parameter, indicated in Table 1 within the Supplemental Material (SM) [58], which integrates the elasticity of each layer (the softer material will accommodate its lattice more). The table also compares the out-of-plane lattice parameters of our heterostructures to their bulk counterparts (using the same methods and pseudopotentials) [3] and to measurements of the vdW gap [59,60].

Figure 2 shows a bar graph comparing the out-of-plane lattice parameters in different conditions: sum of the bulk compounds, of the constrained heterostructures, and the fully relaxed heterostructure calculations. In each case, the calculated out-of-plane lattice parameter, c, can be subdivided into contributions from each individual layer's t and d spacing between the layers. For layers A and B, $c = t_A + t_B + d_A + d_B$ where, for a bulk material, $d_A = d_B$.

Comparing the height of the relaxed heterostructure (right bar in each set of Fig. 2) to the sum of the heights of the bulk compounds first relaxed (left column) then epitaxially constrained (middle) we find there are two groups of materials. In group I (first 4 sets in Fig. 2), there is only a small compression of the out-of-plane lattice parameter (maximum 5%) and most of it is due to strain and the unequal elastic responses of the two materials: For idealized equal and isotropic elastic responses, all of the expansion in A would be a contraction in B and the three bars would be identical. In particular for WS_2/MoS_2 and $MoSe_2/WSe_2$ the lattice constants of Mo and W based TMDs are mainly determined by the chalcogen, and the resulting strain is almost 0.

In group II, there is a strong contraction of the out-of-plane lattice parameter (around 10% on average), and most of the effect is due to the interaction between the layers (change from middle to right bars). The main difference between the two groups is that, in group I the chalcogens of the two

layers are identical ($MoSe_2/WSe_2$, WS_2/MoS_2, TiS_2/ZrS_2, and $TiSe_2/ZrSe_2$) whereas in group II the chalcogens are different ($WS_2/MoSe_2$, WS_2/WSe_2, and $TiS_2/TiSe_2$). Figure 2 shows that the change in out-of-plane lattice parameter is mainly located in a contraction of the vdW gap (d_{vdw}, blue segments). Changes in the geometric thickness (t red and orange segments), on the other hand, are mainly caused by strain. The reason for the interlayer contraction in group II will be explored through several derived properties below. In what follows, we will identify the category of each material using the notation of "symmetry"-"group", i.e., $MoSe_2/WSe_2$ is identified as H-I as the symmetry is hexagonal and it is a group I material.

The compression of the out-of-plane lattice parameter, through the reduction of the vdW gap, leads to important changes in the electronic and vibrational properties of the system. Plots of the Kohn-Sham band structures for each of the compounds are given in Figs. 1 and 2 within the SM [58]. To quantify the change, we compare in Table I the calculated DFT electronic band-gap energies for the heterostructures with the average band-gap energy of the heterostructure components (bulk compound references listed as well). We report band-gap energies for the constrained structures in Table 2 within the SM [58]. Interestingly, within group II, the resulting band-gap energies for all semiconducting heterostructures are smaller than the average and the individual band gaps of their bulk counterparts, whereas the $TiS_2/TiSe_2$ heterostructure becomes semiconducting. Within group I, the average bulk and heterostructure band gaps are comparable. In all of the hexagonal cases, the Q valley between Γ and K is the lowest point in the conduction band (indirect band gap Fig. 1 within the SM [58]), as in the bulk TMD compounds. This will strongly affect the transport and optical properties of the stack, but will also be very sensitive to the precise geometry: A bilayer may be very different from a periodic continuous heterostructure, and strain can invert the valley ordering.

Table I also gives the dielectric tensor ϵ^∞ for both the in-plane and out-of-plane directions for bulk (data from Ref. [3]), ϵ_{xx}^∞ for the bilayer (since the out-of-plane component is ill-defined), and both components for our heterostructures. We find that the out-of-plane dielectric tensor of the heterostructure is larger than the corresponding bulk compounds in group II compounds indicating that there is a greater polarization in the out-of-plane direction. Our bilayer dielectric tensors must be corrected for the increased vacuum spacing in our calculations, as done in Ref. [4]. Briefly, we can account for the increased vacuum spacing by multiplying the dielectric tensor by the ratio of cell volumes (with and without the vacuum spacing).

Given the changes in the lattice parameters of the heterostructures compared to their bulk counterparts, we expect changes in the vibrational structure of these compounds. We use DFPT to calculate the vibrational properties of our systems, determining the interatomic force constants as well as responses to homogeneous electric fields, giving access to the dielectric constant and the Born effective charges (BEC). The interatomic force constants allow us to determine the phonon dispersion relations and related properties (e.g., free energies).

TABLE I. Calculated electronic band-gap energies and electronic contribution to the dielectric tensor (ϵ^∞) for each of our heterostructures and their bulk counterparts. For the heterostructures, we report the category of the material and the average of the host material band gaps. – indicates that the calculated structure is metallic. The values of ϵ^∞ for bulk materials come from Ref. [3] and those of the bilayers come from our calculations after taking into account the quasi-two-dimensional nature of the calculation.

Bulk	E_g (eV)	ϵ_{xx}^∞	ϵ_{zz}^∞
MoS_2	0.886	15.53	6.87
$MoSe_2$	0.853	16.75	8.00
WS_2	1.029	13.82	6.57
WSe_2	0.938	15.39	8.92
TiS_2	–	–	–
$TiSe_2$	–	–	–
ZrS_2	1.041	9.94	5.54
$ZrSe_2$	1.004	14.49	7.06

Bilayer	E_g (eV)	ϵ_{xx}^∞
$MoSe_2/WSe_2$	1.35	14.86
	1.12[a]	
WS_2/MoS_2	1.46	15.10
TiS_2/ZrS_2	0.47	–
$TiSe_2/ZrSe_2$	–	–
$WS_2/MoSe_2$	1.12	17.11
	1.05[a]	
	1.58[b]	
WS_2/WSe_2	1.22	16.51
	1.07[a]	
$TiS_2/TiSe_2$	–	–

Heterostructure	Category	E_{avg} (eV)	E_g (eV)	ϵ_{xx}^∞	ϵ_{zz}^∞
$MoSe_2/WSe_2$	H-I	0.895	0.879	15.97	7.86
WS_2/MoS_2	H-I	0.958	1.049	14.48	6.38
TiS_2/ZrS_2	T-I	–	0.766	16.28	7.05
$TiSe_2/ZrSe_2$	T-I	–	0.159	–	–
$WS_2/MoSe_2$	H-II	0.941	0.722	16.76	9.66
WS_2/WSe_2	H-II	0.983	0.817	15.86	9.25
$TiS_2/TiSe_2$	T-II	–	0.059	–	–

[a]Reference [33] (theory).
[b]Reference [23] (theory).

A. Vibrational Properties

In Figs. 3 and 4 we show the phonon dispersion curves of the heterostructures. We determine the contribution from each layer by projecting the phonon mode displacement vectors onto the atoms in each layer, and color the phonon band structure accordingly. In Fig. 3 we show the phonon dispersion relations for H heterostructures WS_2/MoS_2, $WS_2/MoSe_2$, $MoSe_2/WSe_2$, and WS_2/WSe_2. There is a clear separation between the optical modes from each layer, which is a signature of weak vdW bonding between layers. The only noticeable mixing between the layers occurs in certain acoustic modes near Γ, and avoided crossings, which appear with exchanges of layer character (blue/red switching). In $WS_2/MoSe_2$ (group II), a significantly stronger mixing occurs in the acoustic branches along the in-plane momentum

TABLE II. Frequencies of the interlayer breathing mode (ω_{LBM}) for our commensurate heterostructures. Experimental Raman data for two related structures are shown for comparison.

Heterostructure	Category	ω_{LBM} (cm^{-1})
$MoS_2/MoSe_2$		$\approx$32[a]
$MoSe_2/WSe_2$	H-I	39.8
	bilayer	27.7
WS_2/MoS_2	H-I	49.3
	bilayer	25.0
		31.2[b]
TiS_2/ZrS_2	T-I	33.9
$TiSe_2/ZrSe_2$	T-I	50.1
$WS_2/MoSe_2$	H-II	64.7
	bilayer	46.0
		39[c]
WSe_2/MoS_2		$\approx$32[a]
WS_2/WSe_2	H-II	61.1
	bilayer	65.4
$TiS_2/TiSe_2$	T-II	94.0

[a]Reference [22] (experiment on bilayer).
[b]Reference [24] (experiment on bilayer).
[c]Reference [23] (theory on bilayer).

path. Furthermore, the weak interaction between the layers is supported by small dispersion in the out-of-plane direction (segments Γ-A, K-H, and L-M).

A number of studies have examined the phonon modes of TMD bilayers such as [22–24,62] (our list is not exhaustive and focuses on works with dissimilar chalcogens). In particular Ref. [22] pioneered the field by tracking the Raman shifts in different hetero-bilayer combinations, including WSe_2/MoS_2 and $MoS_2/MoSe_2$. The shear mode disappears in the Raman spectra due to the layer incommensurability (it survives in our calculations due to the enforced epitaxy), but the layer breathing mode is always present, with a frequency between those of the two component bulks, indicating strong mode mixing as we see in this work. Table II compares our calculated interlayer breathing mode frequencies to available literature data. Our frequencies are systematically higher, due to the imposed commensuration and to the periodic nature of our structures out of plane (3D periodicity instead of free bilayers), which will increase the effective interlayer spring constant [62].

In Fig. 4 we present the T heterostructures ($TiS_2/TiSe_2$, TiS_2/ZrS_2, and $TiSe_2/ZrSe_2$), which show a qualitatively different and more complex behavior. The T-heterostructure phonon modes are more strongly hybridized than the H heterostructures (including some optical modes as well), visible in the more numerous mixed magenta bands. There is no splitting between the acoustic and optical manifolds, which is the case in the bulk as well: The bonding is softer than in H-TMDs, with lower optical frequencies and stronger interlayer interactions.

Bulk TiS_2 and $TiSe_2$ are challenging to simulate because they present a charge-density wave (CDW), leading to a phonon instability that is very sensitive to unit-cell volume, pseudopotential, and strain [63–65]. Experimentally and theoretically, the phonon instability in TiS_2 and $TiSe_2$ appears at
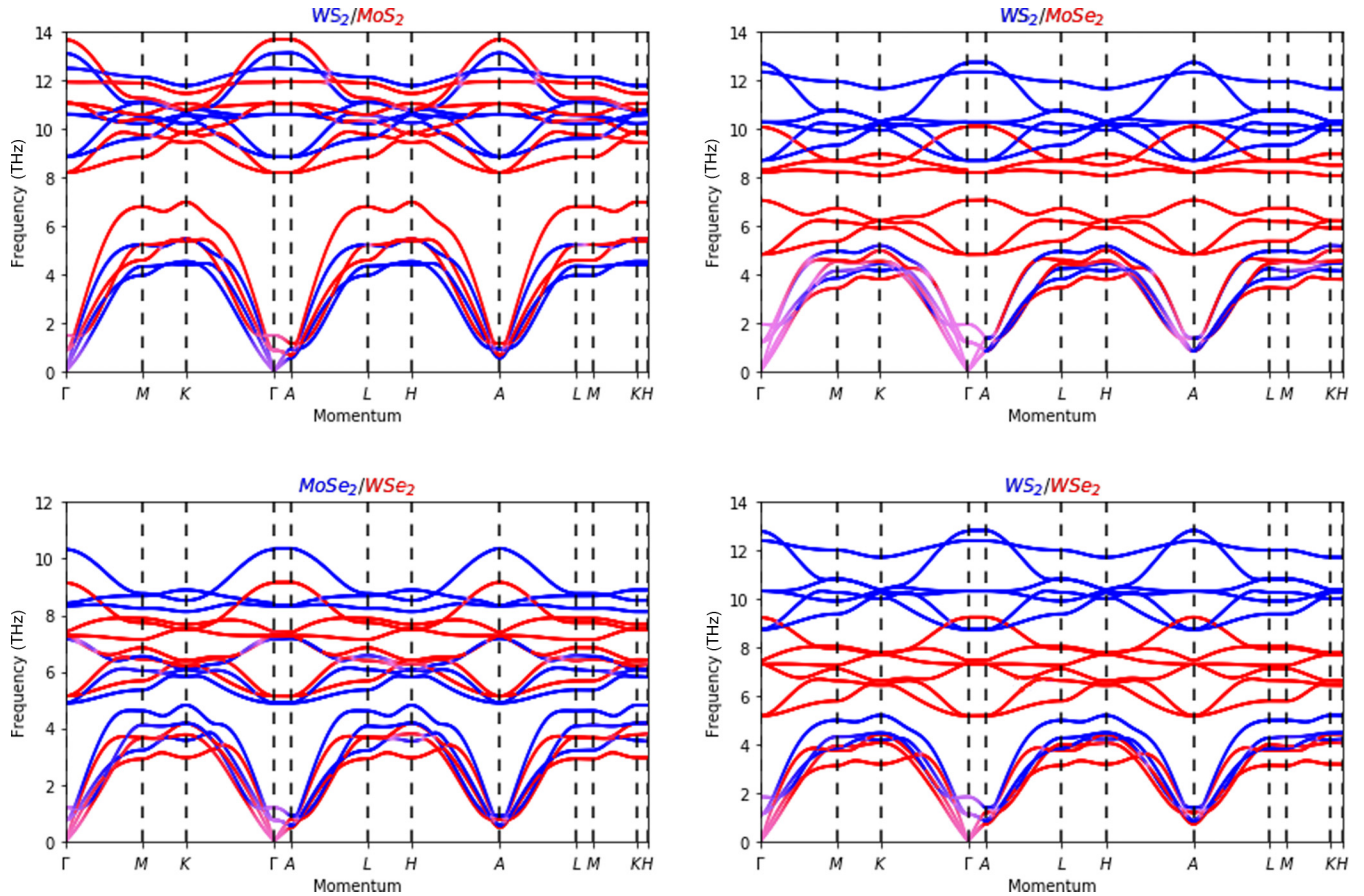
FIG. 3. Phonon dispersion relations for the H heterostructures projected by layer (sum of projected eigendisplacement weight on the atoms in the layer) for group I (WS_2/MoS_2 and $MoSe_2/WSe_2$) and group II ($WS_2/MoSe_2$ and WS_2/WSe_2) heterostructures. The color indicates the fraction of the phonon mode on each layer. Blue: 100% first TMD; red: 100% second TMD; magenta: hybridized mode. The optical modes are very well separated by layer, whereas the acoustic manifold is more mixed, in particular for $WS_2/MoSe_2$. The high-symmetry path in momentum space used for our calculations is shown in Fig. 4.

the M special point for both bulk and ML compounds: The system can gain energy by modulating the charge density and crystal lattice, in a similar way to a Peierls distortion. A review of CDW properties can be found in Ref. [66,67].

For $TiS_2/TiSe_2$, we find that stacking dynamically stabilizes the system: The heterostructure stays metallic, but there are no unstable phonon modes. Recent work by Liao *et al.* [68] shows that, in these CDW materials, induced strain is not enough to stabilize the phonon mode, and that charge transfer is most likely necessary for system stabilization. This is the case for our Ti-based heterostructures as well: There is a net charge transfer between the layers and both layers become doped as shown in Table III (this doping must be reciprocal as the full system is charge neutral). Stabilization via charge transfer is also thought to occur in non-TMD layered materials [21].

We find that TiS_2/ZrS_2 and $TiSe_2/ZrSe_2$ are dynamically unstable: In $TiSe_2/ZrSe_2$ the system remains semi-metallic, and the phonon dynamics preserve the CDW in $TiSe_2$ [64], with an instability at M. For TiS_2/ZrS_2, the band structure becomes semiconducting, and the layers are roughly charge neutral. Here the stronger instability has a different origin, with a Ti-layer optical branch, which is imaginary in the full Brillouin zone. At Γ the two lowest modes are polar in-plane

displacements of the Ti against S, i.e., ferroelectric. Given the experimental demonstration of CDW suppression in heterostructures [21], it would be very interesting if this behavior could be confirmed experimentally as well: 2D ferroelectrics are highly sought after for ultrathin and flexible sensors, actuators, and memory devices. The phonon displacement vectors at M for the lowest imaginary mode are in-plane, with the two S atoms moving in opposite directions along a (110) high-symmetry axis. This is similar to the CDW displacements in bulk, and to the $TiSe_2/ZrSe_2$ instability at M. For the second unstable mode at M, the eigendisplacements follow the (210) in-plane direction. There is a significant out-of-plane component, and a net movement of the $TiSe_2$ layer against the $ZrSe_2$ layer, which produces local Peierls-like dimerization and global buckling of the layers.

B. Origin of the interlayer contraction

A natural explanation for the contraction of the vdW gap would be charge transfer between layers, leading to Coulombic attraction, which is not present in the bulk. A strong charge transfer would make the two layers metallic, with a net electron(hole) excess on layer A(B). This is not the case for the semiconducting TMDs, as the electron band structures
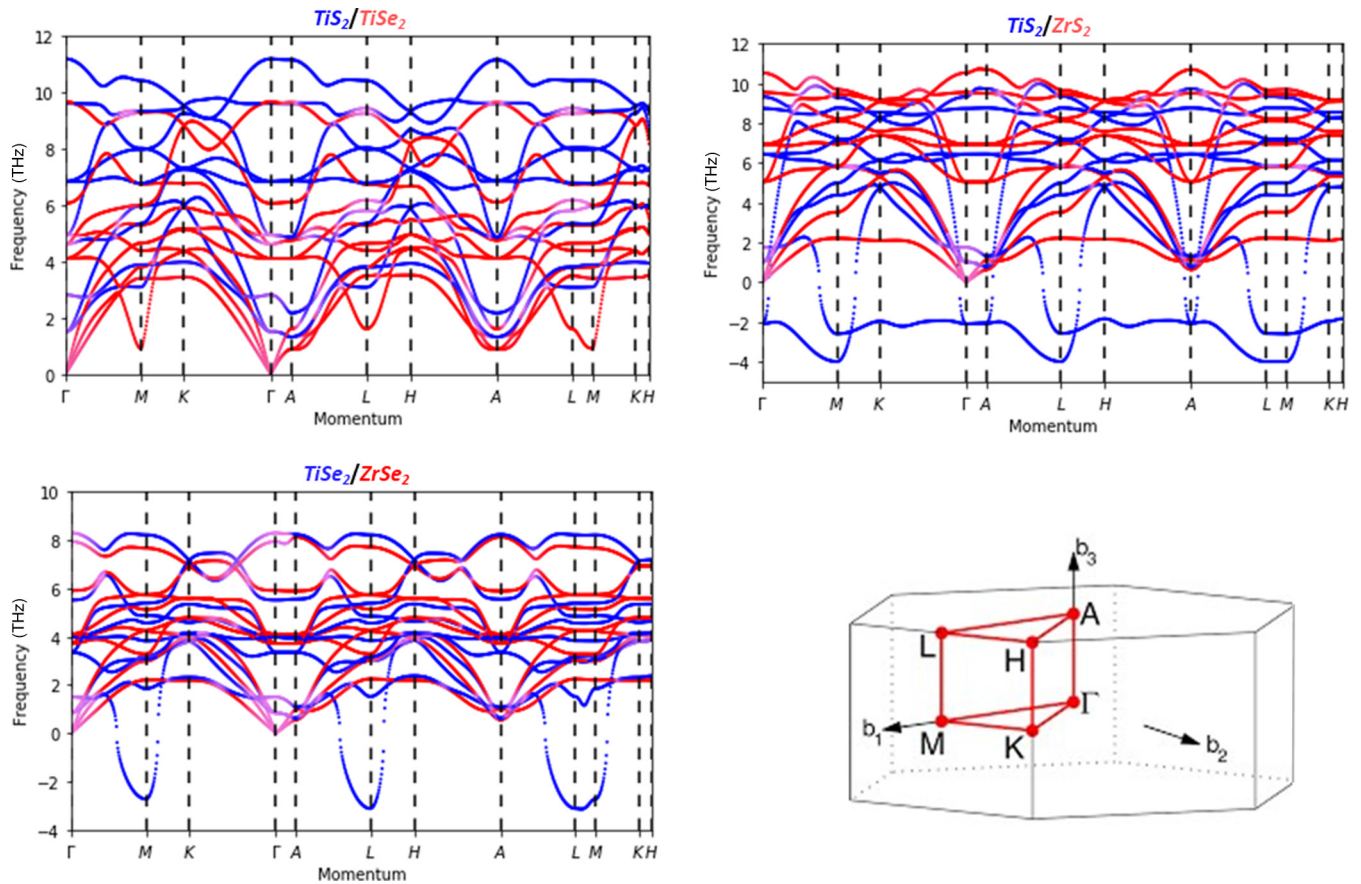
FIG. 4. Phonon dispersion relations of the T heterostructures projected by layer (sum of projected eigendisplacement weight on the atoms in the layer) for group I (TiS_2/ZrS_2 and $TiSe_2/ZrSe_2$) and group II ($TiS_2/TiSe_2$) heterostructures. The color indicates the fraction of the phonon mode on each layer. Blue: 100% first TMD; red: 100% second TMD; magenta: hybridized mode. Lower-right corner: High-symmetry path in momentum space used for our band structure plots from Ref. [61].

show no metallization (see Figs. 1 and 2 within the SM for band structure plots [58]).

A weaker effect would be charge polarization in each layer. To quantify charge transfer and displacement in our heterostructures, we calculate the dynamical (Born) and static (Bader) charges for each atom, compared to the bulk. The dynamical charges are shown in Table III, and systematically increase in the heterostructure environment compared to the bulk. We have highlighted the cells in which there are significant differences (>5%) with respect to the reported bulk BEC in Ref. [3], which happens almost systematically in the out of plane direction. We even find that the BEC of WS_2 in mixed group II heterostructures become larger out-of-plane than in-plane (yellow cells). In hexagonal systems, the counterintuitive sign and abnormal magnitude of the BEC observed in bulk is still apparent even under compression of the unit cell and heterostructure stacking [69]. To characterize the polarization effect in each layer of the group II materials, we calculate the electronic contribution to the dielectric tensor (ϵ^∞) for our heterostructures and compare them to the out-of-plane component of ϵ^∞ of the corresponding bulk compounds in Table I. We find that ϵ_{zz}^∞ of group II heterostructures is larger than their corresponding bulk counter parts. This indicates that the charge transfer induced polarization occurs between the layers rather than within the layer.

For the trigonal compounds, one can not compare to the (metallic) bulk, as the calculated BEC are not meaningful. In semiconducting $TiS_2/TiSe_2$, the large values for Ti atoms are similar to those found, e.g., in oxide perovskites [70]. The large BEC are linked to a sizable dielectric polarizability.

Our calculated values of the static Bader charges, for both bulk and heterostructure systems, are given in Table 3 within the SM [58], and the layer charges (sum of atomic charges for layers A and B), which are shown in the last column of Table III. The charges show small changes with respect to the bulk compounds, but there is a clear difference between the homo-chalcogen cases (few milli-electron charges for the layers) and the hetero-chalcogens (an order of magnitude more), in favor of the sulfide layers.

At this point we have ingredients to understand the shrinking of the interlayer gaps presenting different chalcogens. Changing the bulk environment systematically induces a greater polarizability in both materials, generating additional attractive forces between the layers. The modified charge density gives rise to an induced polarization within the layers, both static (Bader charge imbalance) and dynamic (larger BEC, especially out of plane). The latter is not exclusive to the hetero-chalcogen case, and would mainly be visible in a modification of the phonon frequencies (LO/TO splitting) compared to the bulk. The main effect is therefore the static

TABLE III. Comparison of dynamical and static charges in the TMD heterostructures. The calculated BEC for each of the heterostructures are compared to their bulk counterpart, both in-plane (xx) and out-of-plane (zz). The first column for each BEC direction corresponds to the heterostructure and the second column to the bulk. Shaded cells highlight heterostructure values that differ by more than 5% from the bulk, and yellow cells represent compounds with a larger out-of-plane than an in-plane value of the BEC. – indicates that the calculated structure is metallic. Most of the zz values increase perceptibly, and none of the values decrease: heterostructuring always increases polarizability with respect to a chemically homogeneous reference bulk. The last column contains the static Bader charges, summed over a layer (L) (bulk reference is 0). The heterostructures with identical chalcogens have negligible charge transfer, within the numerical noise of the Bader charge integration routine, whereas the hetero-chalcogen cases show transfers of 0.02 to 0.03 electrons.

		Z^*_{xx}		Z^*_{zz}		
	Atom	het	bulk	het	bulk	$q_{B,L}$(e)
MoSe$_2$/WSe$_2$ H-I	Mo	−1.99	−1.91	−0.99	−0.95	0.000
	Se	1.00	0.95	0.52	0.48	
	W	−1.25	−1.24	−0.80	−0.30	0.008
	Se	0.62	0.62	0.38	0.39	
WS$_2$/MoS$_2$ H-I	Mo	−1.18	−1.09	−0.63	−0.63	0.003
	S	0.59	0.54	0.33	0.31	
	W	−0.52	−0.49	−0.47	−0.43	0.007
	S	0.26	0.25	0.22	0.21	
TiS$_2$/ZrS$_2$ T-I	Ti	−	−	−	−	0.002
	S	−	−	−	−	
	Zr	−	6.19	−	1.82	−0.006
	S	−	−3.17	−	−0.60	
TiSe$_2$/ZrSe$_2$ T-I	Ti	6.63	−	1.03	−	0.011
	Se	−3.24	−	−0.50	−	
	Zr	7.66	6.76	1.89	1.70	−0.007
	Se	−3.90	−4.12	−0.94	−0.55	
WS$_2$/MoSe$_2$ H-II	Mo	−2.02	−1.91	−1.00	−0.95	0.030
	Se	0.96	0.95	0.44	0.48	
	W	−0.49	−0.49	−1.00	−0.11	−0.025
	S	0.26	0.25	0.54	0.21	
WS$_2$/WSe$_2$ H-II	W	−0.48	−0.49	−0.92	−0.11	−0.027
	S	0.26	0.25	0.53	0.21	
	W	−1.32	−1.24	−0.81	−0.30	0.035
	Se	0.65	0.62	0.33	0.39	
TiS$_2$/TiSe$_2$ T-II	Ti	−	−	−	−	−0.032
	S	−	−	−	−	
	Ti	−	−	−	−	0.030
	Se	−	−	−	−	

charge redistribution, polarizing the two layers in opposite ways, and leading to a net compression of the interlayer spacing. The (dispersive) vdW interaction between differing chemical species is not expected to yield this kind of anomaly, and we confirm numerically that the S-Se interaction is simply the average of the S-S and Se-Se (by construction in the Grimme D3 scheme).

A number of recent works (e.g., Refs. [71,72]) have examined Janus TMD structures, where the chalcogen on one side of a layer has been substituted. These can be made experimentally [72] by exposing (e.g.,) MoS$_2$ to a hydrogen plasma and Se vapor. If there are islands or flakes of MoS$_2$ on top of a MoS$_2$ surface, the S against S interface is preserved, and the Janus flake now presents an intrinsic dipole. Epitaxy is enforced by the synthesis process. The interlayer distance is also found to be reduced by this arrangement, as in our calculations. The authors do not specify the mechanism for the layer attraction, but it seems natural to expect it is induced electrostatic as in our work, and not simply vdW interactions. In Ref. [71] bilayers of Janus TMDs are studied theoretically and again the intrinsic dipole leads to an electrostatic attraction/repulsion between the layers: head to tail dipoles yield a smaller interlayer spacing. Again the origin of the contraction observed here and in Janus bilayers is the same.

C. Cross-checks with other van der Waals functionals

Several reviews (e.g., Refs. [73,74]) have compared the performance of different approximations to the vdWs energy contribution, both total energy corrections like Grimme's D3, which we use, and functionals of the density or external reconstructions with Wannier functions or other orbitals. For the structure of TMDs, their performance seems quite equivalent, but we have tested our results on one hexagonal system from group I (MoSe$_2$/WSe$_2$) and one hexagonal system from group II (WS$_2$/MoSe$_2$) using several functionals implemented in VASP [75] with the projector augmented wave method [76]. To confirm the compression in group II structures, we employ the SCAN metaGGA [77,78] and the van der Waals functional rVV10, which together are known to produce good quality results in diversely bonded systems [79]. Comparing SCAN+rVV10 vs PBE-D3, we find that the relaxed bulks and type I MoSe$_2$/WSe$_2$ heterostructure show differences of less than 1% for c lattice parameter and the t and d parameters. For the type II WS$_2$/MoSe$_2$ heterostructure, the c lattice constant is smaller by 4.3% with SCAN+rVV10, but t only changes by 0.6%, so the change is localized in the vdW gap. Analyzing the relaxed structures from each method, we find that the results are consistent with those presented above: considerable interlayer compression (–7.65 and –3.64%, slightly less than with PBE-D3) in group II cases and almost no compression (–0.33 and 0.17%) in group I heterostructures. The heterostructure calculations suggests that SCAN+rVV10 and PBE produce different induced polarizations. This result is consistent with recent work by Zhang *et al.* [80] for ferroelectric materials, where the polarization of the cell is always smaller with SCAN.

V. CONCLUSIONS

In summary, we have calculated the structural, electronic, and vibrational properties of ideal commensurately-stacked heterostructures containing MoS$_2$, MoSe$_2$, WS$_2$, WSe$_2$, TiS$_2$, TiSe$_2$, ZrS$_2$, and ZrSe$_2$ using the ABINIT software package. For dissimilar chalcogen atoms (group II), we find there is a strong contraction of the c lattice parameter, localized in the van der Waals gap distances between the layers. We trace this contraction back to an induced electrostatic effect and a polarization of the layers with a partial spatial charge

transfer, leading to a net attraction between the layers. This effect is disentangled from the artificially imposed epitaxy, by comparing with an intermediate bulk structure, which is constrained in-plane to the heterostructure lattice constant (and relaxed out of plane). For identical chalcogens (group I) there is only a small compression, which is mainly due to the epitaxy.

Calculations of the dynamical stability of these compounds, via the interatomic force constants and the phonon spectra, indicate that the semiconducting heterostructures are stable. In the hexagonal heterostructures there is a clear separation of the optical vibrational modes for each layer, indicating a weaker interlayer interaction in these materials. The acoustic modes mix more, especially in the hetero-chalcogen group II cases. In the trigonal heterostructures, we find that the charge-density wave instability from the Ti = based compounds is affected strongly: Counterintuitively, when one generates a heterostructure of TiS_2 and $TiSe_2$, the resulting compound is dynamically stable due to a small charge transfer between the layers. The TiS_2/ZrS_2 combination is semiconducting with a small gap, but dynamically unstable, with an unstable polar mode at Γ. $TiSe_2/ZrSe_2$ is semimetallic, and retains the CDW instability at the M point of the Brillouin zone. These three evolutions are linked to larger interlayer charge transfers and not only strain, and may be observable in experimental bilayers. Ferroelectricity in TiS_2/ZrS_2 is a particularly exciting possibility.

While these commensurate heterostructures will not all be the experimental ground state (preferring to twist and create moiré patterns), they provide insight into heterostructure property modifications, and guidance to understand how the individual layers change due to stacking in heterostructures. We note several effects, which should be measurable: interlayer distances, phonon frequency shifts, stabilization of charge-density waves ($TiS_2/TiSe_2$), and the appearance of ferroelectricity in TiS_2/ZrS_2. The proximity and layer polarization should also have an impact on transport through the layers. Furthermore, the modification of the distance between the layers has a direct effect on the interlayer electronic coupling and thus increases the moiré superlattice effects on the electronic structure [81,82].

ACKNOWLEDGMENTS

[1] K. S. Novoselov, A. K. Geim, S. V. Morozov, D. Jiang, Y. Zhang, S. V. Dubonos, I. V. Grigorieva, and A. A. Firsov, Science **306**, 666 (2004).

[2] K. S. Novoselov, A. Mishchenko, A. Carvalho, and A. H. C. Neto, Science **353**, aac9439 (2016).

[3] N. A. Pike, A. Dewandre, B. Van Troeye, X. Gonze, and M. J. Verstraete, Phys. Rev. Mater. **2** 063608 (2018).

[4] N. A. Pike, A. Dewandre, B. VanTroeye, X. Gonze, and M. J. Verstraete, Phys. Rev. Mater. **3**, 074009 (2019).

[5] N. R. Wilson, P. V. Nguyen, K. Seyler, P. Rivera, A. J. Marsden, Z. P. L. Laker, G. C. Constantinescu, V. Kandyba, A. Barinov, N. D. M. Hine, X. Xu, and D. H. Cobden, Sci. Adv. **3**, e1601832 (2017).

[6] L. Wang, S. Zihlmann, M.-H. Liu, P. Makk, K. Watanabe, T. Taniguchi, A. Baumgartner, and C. Schönenberger, Nano Lett. **19**, 2371 (2019).

[7] A. Jawaid, J. Che, L. F. Drummy, J. Bultman, A. Waite, M.-S. Hsiao, and R. A. Vaia, ACS Nano **11**, 635 (2017).

[8] G. Iannaccone, F. Bonaccorso, L. Colombo, and G. Fiori, Nat. Nanotechnol. **13**, 183 (2018).

[9] W. Wei, Y. Dai, Q. Sun, N. Yin, S. Han, B. Huang, and T. Jacob, Phys. Chem. Chem. Phys. **17**, 29380 (2015).

[10] F. Chen, Y. Wang, W. Su, S. Ding, and L. Fu, J. Phys. Chem. C **123**, 30519 (2019).

[11] A. Bolotsky, D. Butler, C. Dong, K. Gerace, N. R. Glavin, C. Muratore, J. A. Robinson, and A. Ebrahimi, ACS Nano **13**, 9781 (2019).

[12] W. Zhou, J. Chen, P. Bai, S. Guo, S. Zhang, X. Song, L. Tao, and H. Zeng, Research **2019**, 21 (2019).

[13] M.-Y. Li, C.-H. Chen, Y. Shi, and L.-J. Li, Mater. Today **19**, 322 (2016).

[14] S. Wang, S. Tian, C. Ren, J. Yu, and M. Sun, Sci. Rep. **8**, 12009 (2018).

[15] P. Rivera, J. R. Schaibley, A. M. Jones, J. S. Ross, S. Wu, G. Aivazian, P. Klement, K. Seyler, G. Clark, N. J. Ghimire, J. Yan, D. G. Mandrus, W. Yao, and X. Xu, Nat. Commun. **6**, 6242 (2015).

[16] H. Taghinejad, A. A. Eftekhar, and A. Adibi, Opt. Mater. Express **9**, 1590 (2019).

[17] C. Lattyak, V. Steenhoff, N. Osterthun, M. Vehse, D. Pareek, M. A. Gonzalez, L. Gütay, S. Schäfer, and C. Agert, in *2019 IEEE 46th Photovoltaic Specialists Conference (PVSC)* (IEEE, Chicago, IL, USA, 2019), pp. 1760–1762.

[18] Y. Cao, V. Fatemi, S. Fang, K. Watanabe, T. Taniguchi, E. Kaxiras, and P. Jarillo-Herrero, Nature (London) **556**, 43 (2018).

[19] H. Wang, W. Wei, F. Li, B. Huang, and Y. Dai, Phys. Chem. Chem. Phys. **20**, 25000 (2018).

[20] E. Torun, H. P. C. Miranda, A. Molina-Sánchez, and L. Wirtz, Phys. Rev. B **97**, 245427 (2018).

[21] J.-K. Bao, C. D. Malliakas, C. Zhang, S. Cai, H. Chen, A. J. E. Rettie, B. L. Fisher, D. Y. Chung, V. P. Dravid, and M. G. Kanatzidis, Chem. Mater. **33**, 2155 (2021).

[22] C. H. Lui, Z. Ye, C. Ji, K.-C. Chiu, C.-T. Chou, T. I. Andersen, C. Means-Shively, H. Anderson, J.-M. Wu, T. Kidd, Y.-H. Lee, and R. He, Phys. Rev. B **91**, 165403 (2015).

[23] B. Amin, T. P. Kaloni, G. Schreckenbach, and M. S. Freund, Appl. Phys. Lett. **108**, 063105 (2016).

[24] J. Zhang, J. Wang, P. Chen, Y. Sun, S. Wu, Z. Jia, X. Lu, H. Yu, W. Chen, J. Zhu, G. Xie, R. Yang, D. Shi, X. Xu, J. Xiang, K. Liu, and G. Zhang, Adv. Mater. **28**, 1950 (2016).

[25] N. Mounet, M. Gibertini, P. Schwaller, A. Merkys, I. E. Castelli, A. Cepellotti, G. Pizzi, and N. Marzari, Nat. Nanotechnol. **13**, 246 (2018).

[26] K. Choudhary, I. Kalish, R. Beams, and F. Tavazza, Sci. Rep. **7**, 5179 (2017).

[27] X. Zhang, A. Chen, and Z. Zhou, WIREs Comput. Mol. Sci. **9**, e1385 (2019).

[28] S. Curtarolo, W. Setyawan, G. L. W. Hart, M. Jahnatek, R. V. Chepulskii, R. H. Taylor, S. Wang, J. Xue, K. Yang, O. Levy, M. J. Mehl, H. T. Stokes, D. O. Demochenko, and D. Morgan, Comput. Mater. Sci. **58**, 218 (2012).

[29] B. V. Troeye, A. Lherbier, S. M. M. Dubois, J.-C. Charlier, and X. Gonze, arXiv:1911.06846.

[30] G. Pizzi, S. Milana, A. C. Ferrari, N. Marzari, and M. Gibertini, arXiv:2011.14681.

[31] T. Sohier, M. Gibertini, and M. J. Verstraete, Phys. Rev. Mater. **5**, 024004 (2021).

[32] M. Phillips and C. S. Hellberg, arXiv:1909.02495.

[33] H. Terrones, F. Lopez-Urias, and M. Terrones, Sci. Rep. **3**, 1549 (2013).

[34] G. A. Tritsaris, Y. Xie, A. M. Rush, S. Carr, M. Mattheakis, and E. Kaxiras, J. Chem. Inf. Model. **60**, 3457 (2020).

[35] J. Kang, J. Li, S.-S. Li, J.-B. Xia, and L.-W. Wang, Nano Lett. **13**, 5485 (2013).

[36] M. M. van Wijk, A. Schuring, M. I. Katsnelson, and A. Fasolino, 2D Mater. **2**, 034010 (2015).

[37] C. Zhang, C.-P. Chuu, X. Ren, M.-Y. Li, L.-J. Li, C. Jin, M.-Y. Chou, and C.-K. Shih, Sci. Adv. **3**, e1601459 (2017).

[38] R. M. Martin, *Electronic Structure: Basic Theory and Practice Methods* (Cambridge University Press, Cambridge, 2004).

[39] X. Gonze, Phys. Rev. B **55**, 10337 (1997).

[40] S. Baroni, S. de Gironcoli, A. D. Corso, and P. Giannozzi, Rev. Mod. Phys. **73**, 515 (2001).

[41] X. Gonze and C. Lee, Phys. Rev. B **55**, 10355 (1997).

[42] X. Gonze, G.-M. Rignanese, M. Verstraete, J.-M. Beuken, Y. Pouillon, R. Caracas, F. Jollet, M. Torrent, G. Zerah, M. Mikami, P. Ghosez, M. Veithen, J.-Y. Raty, V. Olevano, F. Bruneval, L. Reining, R. Godby, G. Onida, D. Hamann, and D. Allan, Z. Kristallogr. **220**, 558 (2005).

[43] X. Gonze, B. Amadon, P. M. Anglade, J.-M. Beuken, F. Bottin, P. Boulanger, F. Bruneval, D. Caliste, R. Caracas, M. Cote, T. Deutsch, L. Genovese, P. Ghosez, M. Giantomassi, S. Goedecker, D. Hamann, P. Hermet, F. Jollet, G. Jomard, S. Leroux, Comput. Phys. Commun. **180**, 2582 (2009).

[44] X. Gonze, F. Jollet, F. A. Araujo, D. Adams, B. Amadon, T. Applencourt, C. Audouze, J.-M. Beuken, J. Bieder, A. Bokhanchuk, E. Bousquet, F. Bruneval, D. Caliste, M. Cote, F. Dahm, F. D. Pieve, M. Delaveau, M. D. Gennaro, B. Dorado, C. Espejo, Comput. Phys. Commun. **205**, 106 (2016).

[45] A. H. Romero, D. C. Allan, B. Amadon, G. Antonius, T. Applecourt, L. Baguet, J. Bieder, F. Bottin, J. Bouchet, E. Bousquet, F. Bruneval, G. Brunin, D. Caliste, M. Cote, J. Denier, C. Dreyer, P. Ghosez, M. Giantomassi, Y. Gillet, O. Gingras *et al.*, J. Chem. Phys. **152**, 124102 (2020).

[46] M. Fuchs and M. Scheffler, Comput. Phys. Commun. **119**, 67 (1999).

[47] See https://www.abinit.org/sites/default/files/PrevAtomicData/psp-links/gga_fhi.html for details.

[48] E. J. Walter and A. Rappe, http://opium.sourceforge.net/.

[49] D. R. Hamann, Phys. Rev. B **88**, 085117 (2013).

[50] See https://www.sas.upenn.edu/rappegroup/research/pseudo-potential-gga.html for details.

[51] J. P. Perdew, K. Burke, and M. Ernzerhof, Phys. Rev. Lett. **77**, 3865 (1996).

[52] R. Fletcher, *Practical Methods of Optimization*, 2nd ed. (John Wiley & Sons, New York, 1987).

[53] R. F. W. Bader., Acc. Chem. Res. **18**, 9 (1985).

[54] S. Grimme, S. Ehrlich, and L. Goerigk, J. Chem. Phys. **132**, 154104 (2010).

[55] B. VanTroeye, M. Torrent, and X. Gonze, Phys. Rev. B **93**, 144304 (2016).

[56] R. Sabatini, E. Kucukbenli, C. H. Pham, and S. de Gironcoli, Phys. Rev. B **93**, 235120 (2016).

[57] S. A. Tawfik, T. Gould, C. Stampfl, and M. J. Ford, Phys. Rev. Mater. **2**, 034005 (2018).

[58] See Supplemental Material at http://link.aps.org/supplemental/10.1103/PhysRevB.103.235307, which includes references [3,23,53,59,69], electronic band structure diagrams, and Tables of lattice parameters, electronic band gap values, and Bader charges.

[59] J. Wilson and A. Yoffe, Adv. Phys. **18**, 193 (1969).

[60] J. BENARD and Y. JEANNIN, Investigations of nonstoichiometric sulfides, in *Nonstoichiometric Compounds* (American Chemical Society, Washington, DC, 1963) Chap. 17, pp. 191–203.

[61] W. Setyawan and S. Curtarolo, Comput. Mater. Sci. **49**, 299 (2010).

[62] L. Liang, J. Zhang, B. G. Sumpter, Q. H. Tan, P. H. Tan, and V. Meunier, ACS Nano **11**, 11777 (2017).

[63] K. Dolui and S. Sanvito, Europhys. Lett. **115**, 47001 (2016).

[64] I. B. Guster, E. Canadell, M. Pruneda, and P. Ordejon, 2D Mater. **5**, 025024 (2018).

[65] P. Chen, Y.-H. Chan, X.-Y. Fang, Y. Zhang, M. Y. Chou, S.-K. Mo, Z. Hussain, A. V. Fedorov, and T. C. Chaing, Nat. Commun. **6**, 8943 (2015).

[66] M. Hossain, Z. Zhao, W. Wen, X. Wang, J. Wu, and L. Xie, Crystals **7** 298 (2017).

[67] J. A. Wilson, F. J. D. Salvo, and S. Mahajan, Adv. Phys. **50**, 1171 (2001).

[68] J.-H. Liao, Y.-C. Zhao, Y.-J. Zhao, X.-B. Yang, and Y. Chen, J. Appl. Phys. **127**, 044301 (2020).

[69] N. A. Pike, B. VanTroeye, A. Dewandre, G. Petretto, X. Gonze, G. M. Rignanese, and M. J. Verstraete, Phys. Rev. B **95**, 201106(R) (2017).

[70] P. Ghosez, J.-P. Michenaud, and X. Gonze, Phys. Rev. B **58**, 6224 (1998).

[71] M. Idrees, H. U. Din, R. Ali, G. Rehman, T. Hussain, C. V. Nguyen, I. Ahmad, and B. Amin, Phys. Chem. Chem. Phys. **21**, 18612 (2019).

[72] K. Zhang, Y. Guo, Q. Ji, A.-Y. Lu, C. Su, H. Wang, A. A. Puretzky, D. B. Geohegan, X. Qian, S. Fang, E. Kaxiras,

J. Kong, and S. Huang, J. Am. Chem. Soc. **142**, 17499 (2020).

[73] T. Björkman, A. Gulans, A. V. Krasheninnikov, and R. M. Nieminen, Phys. Rev. Lett. **108**, 235502 (2012).

[74] F. Tran, L. Kalantari, B. Traoré, X. Rocquefelte, and P. Blaha, Phys. Rev. Mater. **3**, 063602 (2019).

[75] G. Kresse and J. Furthmüller, Phys. Rev. B **54**, 11169 (1996).

[76] P. E. Blöchl, Phys. Rev. B **50**, 17953 (1994).

[77] J. Sun, A. Ruzsinszky, and J. P. Perdew, Phys. Rev. Lett. **115**, 036402 (2015).

[78] J. Sun, R. C. Remsing, Y. Zhang, Z. Sun, A. Ruzsinszky, H. Peng, Z. Yang, A. Paul, U. Waghmare, X. Wu, M. L. Klein, and J. P. Perdew, Nat. Chem. **8**, 831 (2016).

[79] H. Peng, Z.-H. Yang, J. P. Perdew, and J. Sun, Phys. Rev. X **6**, 041005 (2016).

[80] Y. Zhang, J. Sun, J. P. Perdew, and X. Wu, Phys. Rev. B **96**, 035143 (2017).

[81] D. A. Ruiz-Tijerina and V. I. Fal'ko, Phys. Rev. B **99**, 125424 (2019).

[82] Y. Wang, Z. Wang, W. Yao, G.-B. Liu, and H. Yu, Phys. Rev. B **95**, 115429 (2017).